The 8th European Congress on Computational Methods in Applied Sciences and Engineering
ECCOMAS Congress 2022
5–9 June 2022, Oslo, Norway

OPENFOAM MODEL OF FLUID-STRUCTURE INTERACTION IN DRY WIRE DRAWING

Mathieu Vervaecke[1,*], Dieter Fauconnier[2,3] and Joris Degroote[1,3]

[1] Department of Electromechanical, Systems and Metal Engineering
Ghent University
Sint-Pietersnieuwstraat 41, 9000 Ghent, Belgium
e-mail: Mathieu.Vervaecke@UGent.be

[2] Department of Electromechanical, Systems and Metal Engineering
Ghent University
Technologiepark Zwijnaarde 46, 9052 Zwijnaarde, Belgium

[3] Flanders Make EEDT-MP, Ghent, Belgium

Key words: Wire drawing, Fluid-Structure Interaction (FSI), OpenFOAM

Abstract.

A fluid-structure interaction model is employed to numerically investigate the interaction between the pressurized thin lubricant film and the radial, plastically deformed steel wire in a dry wire drawing process. A transient simulation is presented, with the implementation of a sliding fluid-structure interaction interface. Moreover, the fluid film has been calculated by the Navier-Stokes equations and the coupling with the wire model is performed by the IQN-ILS technique. This results on the one hand in the monitoring of the stresses and displacements of the structure and on the other hand in an observation of the hydrodynamic pressure build-up and wall shear stresses in the lubricant. Additionally, the evolution of the thickness of the fluid film is presented.

1 INTRODUCTION

Dry wire drawing is a cold work hardening process, where a metallic wire is pulled through a series of dies, in order to progressively reduce its cross-section. A sodium or calcium based soap lubricant is entrained by the wire into the die to reduce friction and energy consumption and to increase the service life of the die, as the surface of the wire and die are separated by a thin lubricant film.

When modeling this process, the elastoplastic deformation of the wire needs to be considered [1, 2], while the die is traditionally assumed to be rigid [2]. The thin lubricant film is typically calculated using the Reynolds equation [1]. The Reynolds equation has been generalized to incorporate variable viscosity as well as variable density and has been proven sufficiently accurate in predicting the film thickness in elastohydrodynamic contact problems. However, for an incompressible piezo-viscous fluid, the Reynolds equation is only able to adequately capture the mechanics of piezo-viscous lubricants if the shear stress is significantly lower than the reciprocal of the pressure viscosity coefficient [3]. In dry wire drawing, the condition of the low shear stress is not fulfilled as this stress can reach extremely high values. Moreover, the Reynolds equation has lower accuracy due to the lack of inertial contributions [4].

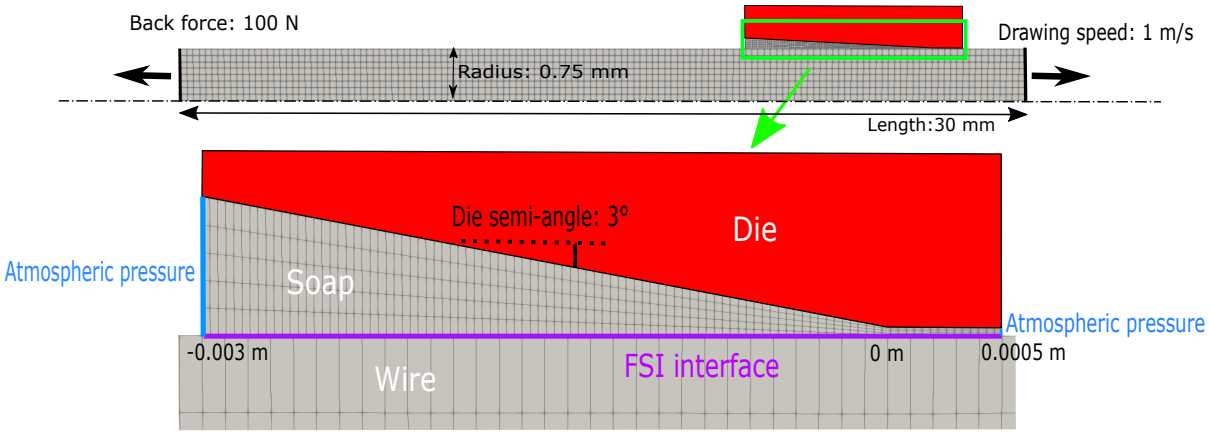

Figure 1: Axisymmetric geometry wire-die configuration before shrinking the die diameter, close up is 5 times scaled radial direction

Hence, the Navier-Stokes equations are used to allow for capturing more accurately the piezo-viscous behavior of the soap in the future [3].

This work presents a 2D axisymmetric fluid-structure interaction (FSI) simulation of dry wire drawing, with the thin lubricant film determined from the Navier-Stokes equations. In current paper we focus on the FSI coupling methodology with the introduction of a *sliding FSI interface*, while assuming for the sake of simplicity a high, but constant viscosity. The piezo-viscous and shear-thinning behavior of the lubricant, with temperature effects will be implemented and investigated in a later phase. The deformation of the structure is calculated by the force balance and the FSI solution is obtained by a partitioned approach [5].

2 METHODOLOGY

This section presents the geometry, boundary conditions and settings of the FSI wire drawing case. Furthermore, the equilibrium conditions on the FSI interface, supported by a flow chart, and the governing equations, with the corresponding discretization schemes for the fluid flow and structure are briefly outlined.

2.1 Geometry, boundary conditions and settings

A wire drawing case consists of a stationary soap granules reservoir, from which soap is entrained, squeezed and liquified between the die and a moving wire (Figure 1). In the presented axisymmetric case, the stationary soap reservoir is not taken into account and the lubricant is approximated as a fluid. To obtain a wire drawing simulation with fluid-structure interaction and a lubricant film, the die diameter is initially expanded with a predefined film thickness and the wire is originally undeformed. During the simulation, the die diameter decreases gradually, while the wire passes through the die and deforms until a new radius is reached. The die is approached as a body with prescribed deformation, while the wire undergoes elastoplastic deformation. Atmospheric pressure is imposed on the inlet and outlet of the lubricant domain.

Table 1: Mechanical properties of the wire

Young's modulus	E	177GPa
Density	ρ	7800 kg/m³
Poisson coefficient	υ	0.3
Initial yield stress	σ_y	1.25GPa
Hardening coefficient		0.3

Table 2: Numerical settings

Number of cells wire		2448
Number of cells lubricant		500
Number of faces wire FSI interface		34
Number of faces lubricant FSI interface		100
Absolute tolerance FSI coupling		0.01 µm
Time step	Δ t	0.0001 s
Total number of time steps		80
Time steps before shrinking die diameter		10
Time steps during shrinking die diameter		70

Following [1] the length of the wire is 30 mm, its diameter is 1.5 mm and the die angle is 6°. A constant tangential velocity of 1 m/s is applied on the outer surface of the wire and represents the wire drawing speed, while the lubricant, with a constant viscosity of 245 Pa.s, has a no slip condition at the boundary with the wire and die. Furthermore, a back force of 100 N is applied as shown in Figure 2. The mechanical properties of the wire are specified in Table 1. Table 2 presents the settings concerning the numerical calculations. The case is solved for time t = [0s, 0.008s]. During the first 10 time steps the die stays on its initial position to avoid numerical instabilities, caused by the acceleration of the wire from 0 to 1 m/s (Figure 1). After these 10 time steps the die diameter starts to shrink each time step, until at time step 80, where a cross-section reduction of 10% of the wire is achieved (Figure 2) [2]. Due to the axial motion of the wire, a sliding FSI interface has to be introduced. A brief explanation concerning the sliding interface is given in section 2.2.1.

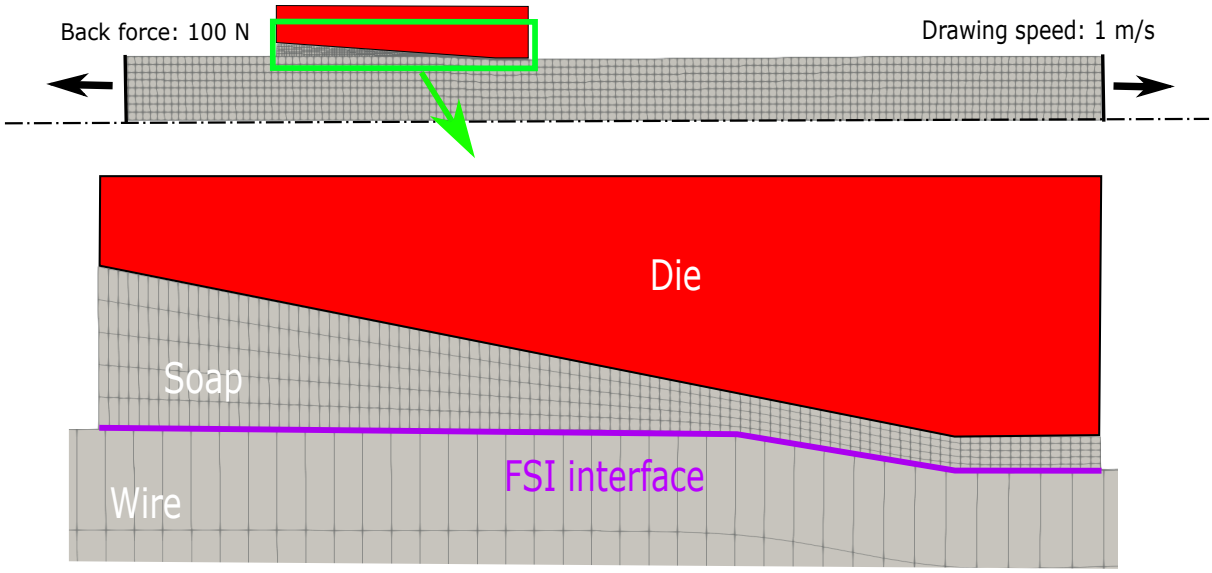

Figure 2: Axisymmetric wire-die configuration after 80 time steps, close up is 5 times scaled in radial direction.

2.2 Solvers (CFD, CSM, FSI)

For the fluid a cell-centered finite volume discretization has been adopted, using pimpleFoam [6] and a Lagrangian solver in OpenFOAM-extend for the structural calculations [7]. The coupling of the flow solver and structural solver is performed by the in-house FSI coupling code CoCoNuT using the quasi-Newton IQN-ILS technique [5, 8].

2.2.1 FSI solver

Generally, an FSI problem consists of a fluid domain Ω_f and a structural domain Ω_s. The boundaries of both domains are indicated as Γ_f and Γ_s, respectively. The intersection of these boundaries is defined as the fluid-structure interaction interface and denoted as $\Gamma_i = \Gamma_f \bigcap \Gamma_s$. The fluid-structure interaction interface (FSI interface) is indicated in Figure 1 and Figure 2 with the purple line.

In order to obtain an FSI solution, two equilibrium conditions have to be fulfilled. The first one is the kinematic condition, where the fluid velocities must be equal to

$$\vec{v_f} = \frac{D\vec{u_s}}{Dt} \tag{1}$$

for all points on the interface, and the second one is the dynamic condition, where the forces must be equal to, but opposite in sign (3^{th} Newtonian law)

$$\sigma_f \cdot \vec{n_f} = -\sigma_s \cdot \vec{n_s} \tag{2}$$

for all points on the interface. Vector $\vec{v_f}$ represents the fluid velocity, $\vec{u_s}$ the structural displacement vector and t the time. σ is the stress tensor and $\vec{n}$ is the unit normal vector pointed outwards from the domain Ω. The flow equations are solved for a given velocity. The velocity boundary condition is obtained by the time derivative of the displacement on the fluid-structure interface as stated in Equation 1. Furthermore, a traction vector is imposed on the fluid-structure boundary of the structure domain.

The flow and structure are briefly written by $F(x)$ and $S(y)$, respectively. The displacements are represented by x, while y gives the loads on the fluid-structure interface. The dependency on previous time steps and on the variables outside the interface are not covered by this notation. The output of a solver is denoted with a tilde,

$$\widetilde{y}_{k+1} = F(x_{k+1}) \tag{3}$$

$$\widetilde{x}_{k+1} = S(y_{k+1}) \tag{4}$$

where *k+1* represents the coupling iteration.

During the simulation, the lubricant Ω_f stays fixed in the axial direction, while the wire Ω_s moves along the axisymmetric axis (Figure 1 and 2). This creates a large translation of the structural domain with respect to the fluid domain in axial direction. A technique to deal with large translations or rotations is a sliding interface [5]. This implies for every edge or face on one side, the overlapping edges or faces on the other side are searched and projected on each other. This projection is subsequently used

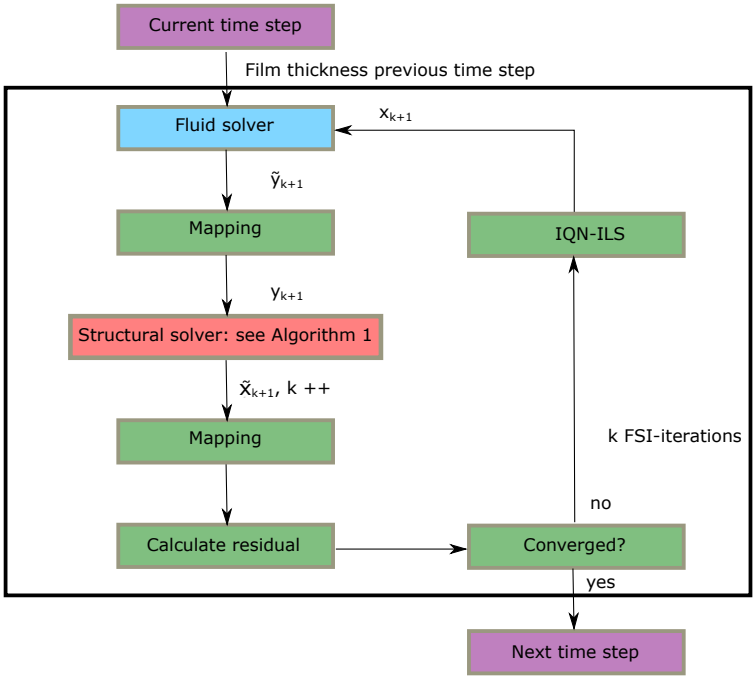

Figure 3: Flow chart FSI wire drawing

to interpolate data from one side to the other side. The technique of a sliding interface has, among other things, been used in simulations of wind turbines, where a rotating and stationary fluid domain are separated by sliding interfaces [10]. Unlike [10], where the sliding interface is implemented in the fluid domain, the present case applies a sliding FSI-interface. When the wire moves through the die, the hydrodynamic pressure and wall-shear stresses calculated by the fluid solver have to be imposed on the correct position on that part of the wire located in the die. On the other hand only the grid velocity normal to the interface has to be the same on both sides of the interface, which allows slip of the fluid grid with respect to the structure grid, even though the boundary has a no-slip condition [5]. Consequently, the intersection Γ_i has to be updated each time step.

Figure 3 presents the flow chart of the wire drawing FSI calculation. The colors blue, green and red give the distinction between the calculations executed in the fluid solver, FSI solver and structural solver, respectively. In this case, the mesh at the coupling interface on the fluid side is different compared with the mesh of the structure at the FSI interface (Figure 1 and 2). As presented in Figure 3 mapping is executed from the fluid solver to the structural solver and vice versa, to execute the required transfer of data from Γ_f to Γ_s and the other way around. Both mapping blocks contain an axisymmetric to 2D and 2D to axisymmetric mapper, with a linear interpolation of both grids. This is introduced to obtain a sufficient quality of the FSI interface. Furthermore, the residual r of the FSI-loop is calculated as

$$r_{k+1} = S \circ F(x_{k+1}) - x_{k+1} \tag{5}$$

Convergence is reached when $\|r\|_2 \leq \varepsilon_x$, with ε_x the absolute convergence tolerance (Table 2) [8].

2.2.2 CFD solver

During the simulations the mesh of the fluid film will deform and hence the Arbitrary-Euler-Lagrange (ALE) formulation is used. The conservation of mass and the momentum equations are given by

$$\frac{\delta}{\delta t}\int_{V_f}\rho_f\,\mathrm{d}V_f+\oint_{S_f}(\vec{v_f}-\vec{v_{fg}})\cdot\vec{n_f}\,\mathrm{d}S_f=0 \tag{6}$$

$$\frac{\delta}{\delta t}\int_{V_f}\rho_f\vec{v_f}\,\mathrm{d}V_f+\oint_{S_f}(\rho_f\vec{v_f}\otimes(\vec{v_f}-\vec{v_{fg}}))\cdot\vec{n_f}\,\mathrm{d}S_f=\oint_{S_f}\sigma_f\cdot\vec{n_f}\,\mathrm{d}S_f \tag{7}$$

where V_f is the volume and S_f the surface of the cell. The flow velocity is represented by $\vec{v_f}$, $\vec{v_{fg}}$ is the grid velocity, ρ_f the fluid density and t the time. To compute the grid velocity the so-called *space conservation law (SCL)* [9] is applied.

$$\frac{\delta}{\delta t}\int_{V_f}\mathrm{d}V_f-\oint_{S_f}\vec{v_{fg}}\cdot\vec{n_f}\,\mathrm{d}S_f=0 \tag{8}$$

Substituting Equation 8 in Equation 6 gives the continuity equation for an incompressible and isothermal flow:

$$\oint_{S_f}\vec{v_f}\cdot\vec{n_f}\,\mathrm{d}S_f=0 \tag{9}$$

In this case the fluid is approximated as a Newtonian fluid, so the stress tensor is defined as $\sigma_f = -p\mathbf{I}$ $+2\mu_f D$, where p is the pressure, μ_f the fluid viscosity and $D = \frac{1}{2}[\nabla\otimes\vec{v_f}+(\nabla\otimes\vec{v_f})^T]$ the rate of strain tensor. The first term of the left hand side of Equation 7 is discretized with a first order accurate scheme to provide higher numerical stability. The Peclet number is significantly lower than 1, which allows to apply a second order central discretization scheme on the convection term (second term left hand side of Equation 7), which gives a higher accuracy. The term on the right hand side of Equation 7 is discretized with a second order central scheme as well.

2.2.3 CSM solver

Considering an arbitrary body of volume V_s bounded by a surface S_s, the governing equation is given by the force balance and is denoted as

$$\frac{\delta}{\delta t}\int_{V_s}\rho_s\vec{v_s}\,\mathrm{d}V_s=\oint_{S_s}\sigma_s\cdot\vec{n_s}\,\mathrm{d}S_s \tag{10}$$

where ρ_s presents the solid density, $\vec{v_s}$ the velocity vector and σ_s the Cauchy tensor of the structure. Moreover, the relation between the stress tensor σ_s and the strain is given by the constitutive equation of the material and are defined in detail in [7]. To allow a segregated solution procedure, the surface force (first term right hand side Equation 10) is partitioned into implicit and explicit components. This procedure is described in [7, 11] and gives:

$$\begin{aligned}\int_{V_s}\frac{\delta}{\delta t}(\rho_s\frac{\delta(\vec{u_s}^{m-1}+\Delta\vec{u_s}^{e})}{\delta t})\,\mathrm{d}V_s=&\oint_{S_s}((\frac{4}{3}\mu_s+K)\vec{n_s}\cdot\nabla(\Delta\vec{u_s}))^e\,\mathrm{d}S_s+\oint_{S_s}((j\mathbf{f}^{-T}\cdot\vec{n_s})\sigma_s)^{e-1}\,\mathrm{d}S_s\\&-\oint_{S_s}((\frac{4}{3}\mu_s+K)\vec{n_s}\cdot\nabla(\Delta\vec{u_s}))^{e-1}\,\mathrm{d}S_s\end{aligned} \tag{11}$$

where $\vec{u_s}$ is the displacement vector of the structure, μ_s the shear modulus, K the bulk modulus, $\mathbf{f}$ the relative deformation gradient and j the Jacobian of the relative deformation gradient. Furthermore, the relative deformation gradient is described in terms of the displacement increment as $\mathbf{f} = \mathbf{I} + \nabla(\Delta\vec{u_s})^T$. The displacement increment is given by $\Delta\vec{u_s} = \vec{u_s}^m - \vec{u_s}^{m-1}$. The subscripts m and $m-1$ indicate values of current and previous time step and the subscripts e and $e-1$ indicate values of the current and previous iteration of the structural solver, respectively. The components containing $\vec{u_s}^{m-1}$ and $\Delta\vec{u_s}^e$ of the first term at the left hand side of Equation 11 are discretised using a first-order accurate backward differencing scheme. The first term at the right hand side of Equation 11 is discretised using central differencing with over-relaxed non-orthogonal correction. The second and third terms on the right-hand side of Equation 11 are discretised using central differencing as well. Recall that the first term and the third term of Equation 11 do not exactly cancel out, because the first term is treated implicitly, while the third term is approximated explicitly. The difference of both terms results in additional numerical diffusion, which tends to eliminate erroneous oscillations. The complete and detailed formulation of the structural solver, with the numerical implementation is described in [7, 11].

Originally, the structural solver was created for simulation of metal forming processes without interaction with a fluid [7]. During plastic wire deformation, work hardening occurs. Consequently to achieve true stress, the yield stress field and the mesh grid have to be updated each time step. This means the result of the current time step is depending on the result simulated in the previous time step. For this reason, during an FSI calculation the yield stress field and the mesh have to be reset to the values of the previous time step before the structural calculation is executed in each coupling iteration of the current time step. Hence, the structural solver has been adapted, to reset the mesh and yield stress field. The algorithm of the source code with the adjustments is given by Algorithm 1. The executed modifications compared to [7] in Algorithm 1 are indicated by the *italic* text. The residual r_s of the structural solver is calculated by

$$r_s = \frac{\|\Delta\vec{u_s}^e - \Delta\vec{u_s}^{e-1}\|_\infty}{\|\Delta\vec{u_s}^e\|_\infty} \tag{12}$$

where e and $e-1$ are the current and previous structural solver iterations, respectively. Convergence is reached when $r_s \leq \zeta$, with ζ the convergence tolerance equal to $4e-9$.

Algorithm 1 Solution procedure structural solver FSI modification

```
1:  for all time steps do
2:      for each FSI coupling iteration do
3:          Reset mesh to mesh of previous time step.
4:          Reset yield stress field to yield stress field of previous time step.
5:          while ζ is not reached do
6:              Momentum equation: assemble and solve in terms of Δu_s. See [7]
7:              Update kinematics and stress. See [7]
8:          end while
9:          Interpolate cell-centre displacements to the vertices.
10:         Move mesh to deformed configuration using the vertex displacements.
11:     end for
12: end for
```

3 RESULTS

The results section first describes the physical and then the convergence results. Figure 4 represents the equivalent Cauchy stress at the top surface of the wire. The equivalent Cauchy stress is the six directional components turned into a single number which can be compared to a uniaxial measure of yield [12]. At the initial condition, the equivalent Cauchy stress on the top surface of the wire is located under the initial yield stress of 1.25 GPa (left graph Figure 4), which means that the wire deforms only elastically. The right graph of Figure 4 presents the yield stress and the equivalent Cauchy stress under plastic deformation conditions, i.e. at decreased die diameter. A significant difference is observed concerning the shape and magnitude of the equivalent Cauchy stress at the wire surface. The steep increase of the stresses are limited by the yield stress around the middle of the domain, where plastic deformation occurs and work hardening on the wire is achieved.

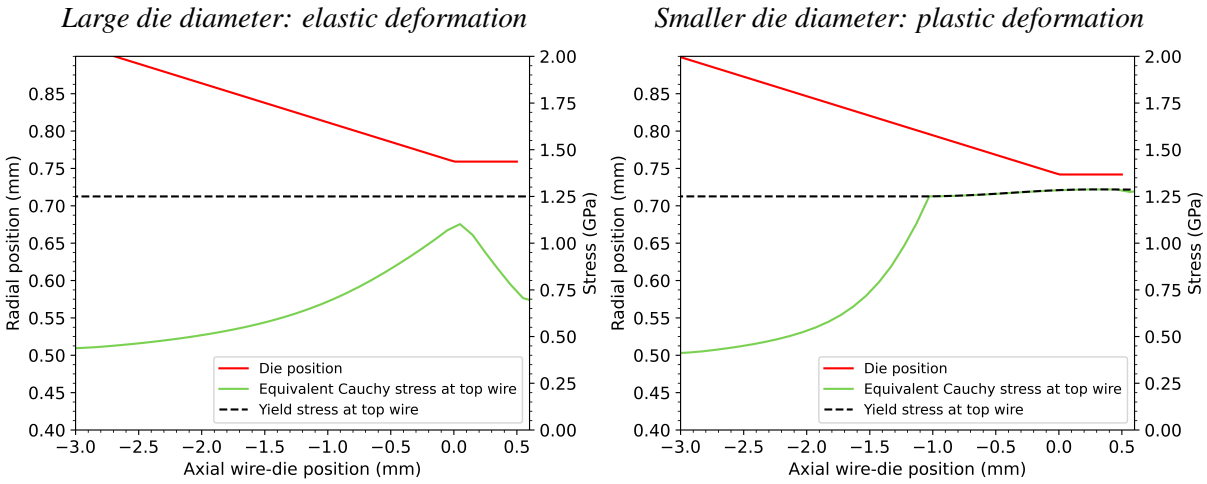

Figure 4: Comparison equivalent Cauchy stress and yield stress before and after die diameter reduction

Figure 5 presents two graphs with the film thickness of the soap and the radial displacement of the wire before and after shrinking the die diameter. As stated before, during the die diameter decrease, the wire starts to deform plastically. Consequently, an increase of the fluid film thickness with a significant higher radial displacement is observed at the right graph of Figure 5. When the wire leaves the die, the wire is exposed to a limited elastic recovery. Contrary to the right graph of Figure 5, its left graph shows a quasi constant film thickness in the narrow gap between wire and die with a small radial displacement and a complete elastic recovery after the wire has left the die. Note however that this simulation covers an extremely limited time span and steady state is not yet obtained. This means the shape and thickness of the fluid film are probably showing a transient behavior.

The pressure distribution, presented in the left graph of Figure 6, illustrates a similar shape as the expected pressure distribution under a tapered land bearing [13]. The highest peak is situated at the narrow gap between wire and die. After shrinking the die (right graph Figure 6) it is noted that the pressure distribution shape and magnitude are changed. The pressure peak is shifted towards the entrance of the die and is slightly higher. Moreover, the peak is less sharp compared with the initial case, due to the

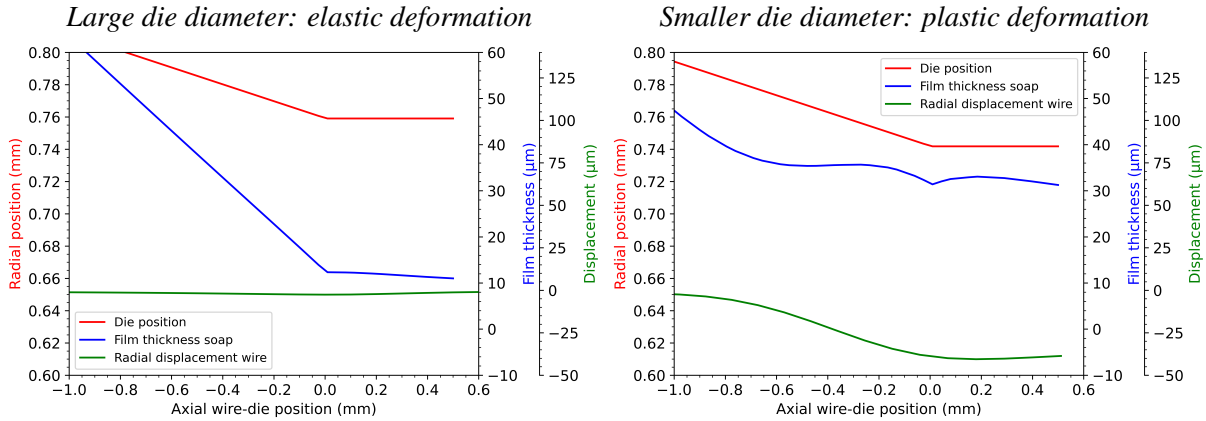

Figure 5: Comparison radial displacement wire and film thickness soap before and after die diameter reduction

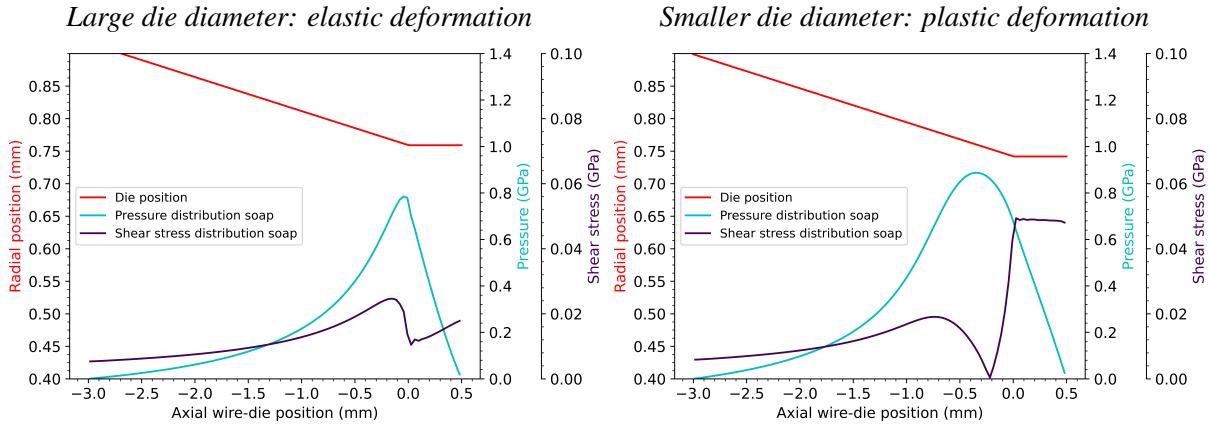

Figure 6: Comparison load distributions soap before and after die diameter reduction

smooth deformation of the surface. Additionally, a significant increase of the shear stress is noticed at the narrow gap of the die and wire when the die achieved its predefined final position (right graph Figure 6). As mentioned earlier, current transient CFD-FSI calculation involve a small wire-length, which appears to be insufficient to obtain steady state conditions for pressure and stress distributions as well as the film thickness distribution.

At last, Figure 7 displays the residuals of the last 5 time steps. Each blue dot represents an FSI coupling iteration, with the calculated residual. For each time step, the FSI tolerance of 0.01 µm has been reached and presents a converged solution. The averaged number of FSI-iterations per time step is 5.33, which indicates a good performance of the IQN-ILS solver [8].

4 CONCLUSION

This paper presents a 2D axisymmetric simulation of wire drawing with a successful implementation of a sliding interface. The sliding interface is a well known technique in the field of computational fluid dynamics, which is to our knowledge applied for the first time on the fluid-structure interaction interface in a wire drawing simulation. An additional innovation in the current case is the use of the Navier-

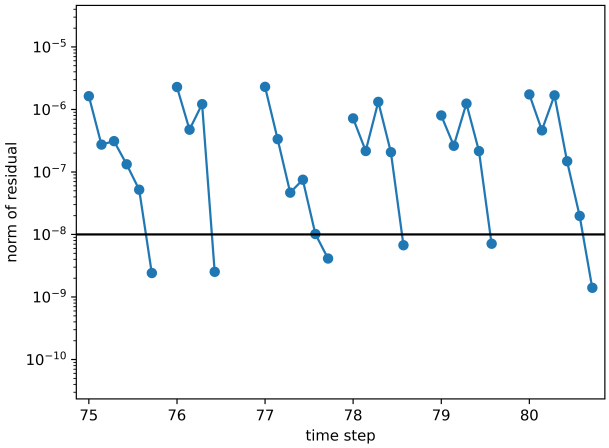

Figure 7: Residuals FSI calculation last 5 time steps before reaching wire cross-section reduction of 10 percent

Stokes equations to capture the behavior of the lubricant film. Moreover, this case shows a converged solution with plastic deformation of 10% cross-section reduction of a steel wire. The coupling between the fluid solver and the modified structural solver is achieved using a partitioned approach with the quasi-Newton technique IQN-ILS. By shrinking the die diameter during the simulation, the predefined cross-section reduction of the wire is attained. The fluid-structure interaction between the wire and the lubricant elucidates a clear distinction of the physical parameters before and after shrinking the die diameter. It has been shown that the equivalent Cauchy stress at the wire surface is limited by the value of the updated yield stress after shrinking the die. Additionally, at the initial state a small increase of the film thickness is observed, corresponding with a small radial displacement of the wire, followed by a complete elastic recovery when the wire leaves the die. However, when the die diameter is decreased, a significant increase of the lubricant film thickness is noticed with a high radial displacement of the wire, followed by a limited elastic recovery. Moreover, the pressure distribution of the fluid film is evolving from a sharp peak situated at the narrow gap between the wire and die, towards a slightly higher, blunt top, which is moved to the entrance of the die. Note however that the time span after reaching the 10 % cross-section reduction of the wire is extremely short to define these results as steady state, due to the limited length of the wire. Furthermore, the viscosity of the fluid film is approximated as constant, which means that the physical representation and behavior of the discussed soap parameters have to be improved to formulate a strong conclusion about film thickness, pressure and shear stress distribution of the lubricant during wire drawing.

To achieve a steady state solution, wire layering will be applied, which is work in progress. An additional advantage of implementing wire layering is the improvement of the calculation time of this case. Further future upgrades will focus on the temperature effects, shear-thinning and piezo-viscous behavior of the soap. Finally, the aim is to validate the numerical results with experimental data.

5 ACKNOWLEDGMENTS

The authors gratefully acknowledge financial support from NV Bekaert SA, Belgium through Dr. Stijn De Pauw.

REFERENCES

[1] Skuric, V., De Jaeger, P., Jasak, H., Lubricated elastoplastic contact model for metal forming processes in OpenFOAM, *Elsevier, compfluid. (2018)*, **172**: 226-240

[2] Hwang, J., Son, I., Yoo, J., Zargaran, A., Kim, N., Effect of reduction of area on microstructure and mechanical properties of twinning-induced plasticity steel during wire drawing, *Met. Mater. Int (2015)*, **21**: 815-822.

[3] Bair, S., Khonsari, M., Winer, W.O., High-pressure rheology of lubricants and limitations of the Reynolds equation, *Elsvier, Tribology International (1998)*, **31**: 3323-3341.

[4] Scurria, L., High-fidelity modeling of elastohydrodynamically lubricated contacts for system-level simulations, *Doctoral dissertation submitted to obtain the academic degree of Doctor of Electromechanical Engineering, Ghent University*, 2021, ISBN 978-94-6355-557-9.

[5] Degroote, J., Partitioned simulation of fluid-structure interaction, Coupling Black-Box Solvers with Quasi-Newton Techniques, *Arch Comput Methods Eng (2013)*, **20**: 185-238.

[6] Holzmann, T., Mathematics, numerics, derivations and OpenFOAM, The basics for numerical simulations, *Holzmann CFD*, Release 7.0, URL https://Holzmann-cfd.de, DOI: 10.13140/RG.2.2.27193.36960.

[7] Cardiff, P., Tukovic, Z., De Jaeger, P., Clancy, M., Ivankovic, A., A Lagrangian cell-centred finite volume method for metal forming simulation, *Int. J. Numer. Meth. Engng (2017)*, **109**: 1777-1803.

[8] Delaissé, N., Demeester, T., Fauconnier, D., Degroote, J., Surrogate-based acceleration of quasi-Newton techniques for fluid-structure interaction simulations, *Elsevier, Computers and Structures (2021)*, **260**: 106720, pp.21.

[9] Breuer, M., De Nayer, G. Münsch, M., Gallinger, T., Wüchner, R., Fluid-structure interaction using a partitioned semi-implicit predictor-corrector coupling scheme for the application of large-eddy simulation, *Elsevier, jfluidstructs. (2011)*, **29**: 107-130.

[10] Santo, G., Peeters, M., Van Paepegem, W., Degroote, J., Effect of rotor-tower interaction, tilt angle, and yaw misalignment on the aeroelasticity of a large horizontal axis wind turbine with composite blades, *John Willey and Sons, Ltd. (2020)*, **23**: 1578-1595

[11] Cardiff, P., Karac, A., Ivankovic, A., A large strain finite volume method for orthotropic bodies with general material orientations, *Elsevier, Comput.Methos Appl.Mech.Engrg (2014)*, **268**: 318-335.

[12] de Souza Neto, EA., Peric, D., Owen, DRJ., Computational methods for plasticity: theory and applications, Wiley, 2011, New York

[13] van Beek, A., Advanced Engineering Design, Lifetime performance and reliability, *TU Delft*, ISBN-10: 90-810406-1-8.